

Partial and Contingent Recoil-Frame Covariance-Map Imaging

David Heathcote and Claire Vallance*

*Department of Chemistry, University of Oxford, Chemistry Research
Laboratory, 12 Mansfield Rd, Oxford OX1 3TA, UK*

*e-mail: claire.vallance@chem.ox.ac.uk

Abstract

When applied to multimass velocity-map imaging data, covariance analysis reveals correlations between different fragment ions formed from the same parent molecule, and can provide detailed insights into the fragmentation dynamics. Covariances between the time-of-flight signals for two different ions show that they are formed in the same event, while covariances between their velocity-map images, often referred to as 'recoil-frame covariances', reveal details of the correlated motion of the two fragments. In many cases, covariance analysis is complicated by the fact that fluctuations in experimental parameters such as laser or molecular beam intensities can lead to apparent correlations between unrelated ions. In the context of time-of-flight covariance signals, this problem has been overcome by the introduction of partial covariance and contingent covariance approaches. Here, we apply these approaches to recoil-frame covariance-map images. We also demonstrate that in many cases the total signal within each experimental cycle can be used as a useful proxy for independent explicit measurements of the varying experimental parameter(s).

1 Introduction

The key aim of a molecular reaction dynamics study is to understand the detailed mechanism linking reactants to products, usually in terms of the pathway traversed by the system across one or more potential energy surfaces. Experimental and theoretical capabilities have advanced dramatically in recent years, leading to an increase in size of the chemical systems that can be studied in this way. Larger systems have correspondingly more complex dynamics, often involving multiple competing reaction pathways, and require new experimental and data analysis techniques in order to elucidate the various possible chemical outcomes. In our own work, we employ multi-mass velocity-map imaging to

record scattering distributions for each product of a photoinitiated or electron-initiated reaction within a single measurement. In systems involving multiple fragmentation pathways, it is not always straightforward to identify pairs of co-fragments arising from distinct fragmentation pathways based solely on inspection of the velocity-map images. In such cases, covariance analysis - which reveals statistical correlations between fragments - can be an extremely helpful approach.¹⁻¹¹ We note that when combined with Coulomb-explosion imaging, covariance analysis can also provide direct structural and alignment information on isolated molecules and molecules and molecular complexes embedded in helium nanodroplets.^{6,7,11-14}

The correlations of most interest in all of these applications are correlations between the time-of-flight signals,²⁻⁴ which reveal the product identities, and between the product recoil velocities,⁵⁻¹⁰ which reveal the product dynamics. Provided that each molecule undergoing the process under study can be considered independently of one another, fragment ions produced from different molecules will not correlate with one another. Thus, covariance analysis allows us to isolate processes in which two or more ions are formed from the same parent molecule, often against a large background of uncorrelated events. Time-of-flight covariance signals reveal which pairs of fragments are formed together as co-fragments, while recoil-frame covariance shows how their velocity vectors are correlated with each other. Our implementation of recoil-frame covariance, described in more detail in Section 2.1.2, allows the velocity distribution of a chosen ‘signal’ ion to be determined relative to that of a second, ‘reference’ ion, whose velocity vector has been fixed to lie along a selected axis. To give a simple example, in a two-body dissociation, the two reaction products must travel in opposite directions with equal momenta. In the recoil-frame covariance image, the covariance signal would therefore appear as a well-resolved peak at 180 degrees from the velocity vector of the reference ion.

Whilst covariance analysis performs very well when the experimental conditions are perfectly stable, it is rare for this to be the case, and fluctuations in experimental parameters such as beam intensities can complicate the interpretation of covariance signals considerably by introducing so-called ‘false covariances’. To understand the source of these false covariance signals, consider a photoionisation experiment in which the laser power fluctuates significantly on a shot-to-shot basis. When the laser power is low, the signal for all ions is low, and when the laser power is high, the signal for all ions is increased. This causes the intensity of all ion signals to be correlated with the intensities of all

other ion signals, with the fluctuations introduced by the laser instability often outweighing the ‘true’ covariance signals caused by dynamical correlations between the ions. In this situation, if the laser fluctuations are sufficiently small, covariance analysis may still work well. However, for larger fluctuations the false covariances may dominate and mask the ‘true’ covariances arising from the photoionisation dynamics.

To overcome such complications, two variants on ToF covariance have been introduced, namely partial ToF covariance,^{4,15,16} and contingent ToF covariance.¹⁷ Both require some measured experimental parameter which is used to quantify the fluctuation leading to the false covariance, generally the laser power for each acquisition cycle. Here, we demonstrate the extension of these variants to recoil-frame covariance, and also show that it is not always necessary to measure a varying parameter directly.

2 Methods

2.1 Covariance analysis

2.1.1 Covariance

As already stated, covariance is a statistical measure of the correlation between two variables, denoted X and Y in the following. Mathematically, the covariance between these two variables is described by the following equation:^{2,18}

$$\begin{aligned}\text{cov}(X, Y) &= \langle (X - \langle X \rangle) (Y - \langle Y \rangle) \rangle \\ &= \langle XY \rangle - \langle X \rangle \langle Y \rangle\end{aligned}\tag{1}$$

where $\langle X \rangle$ indicates the mean of X . Inspecting the first line of Equation 1, we see that if when X is larger than its mean value, Y also tends to be larger than its mean value, the covariance will be positive and X and Y are said to be correlated. Conversely, if when X is larger than its mean value, Y tends to be smaller than its mean value, the covariance will be negative and the two values are said to be anticorrelated. If the covariance is zero then there is no correlation between the two parameters.

2.1.2 Calculation of time-of-flight and recoil-frame covariance

In a multi-mass velocity-map imaging experiment, each ion signal yields an (x, y, t, n) data point, where (x, y) are the spatial coordinates of the ion at the detector, t is the arrival time of the ion at the detector (which can be converted to the mass-to-charge ratio m/z for the ion), and n is the number of the experimental acquisition cycle within which the ion was detected.

To determine the time-of-flight (ToF) covariance, we calculate the covariance between the measured fragment ToF spectrum and itself. We note that since correlated ions are formed in the same chemical event, they must arrive within the same experimental acquisition cycle. Therefore, for each acquisition cycle the covariance is calculated between each pair of time points in the ToF spectrum, with the averages in Equation 1 being performed over the number of experimental cycles. The resulting two-dimensional covariance matrix can be plotted in the form of a covariance map, examples of which can be seen in Figure 1. The covariance maps show a line of ‘auto-covariance’ along the diagonal, corresponding to the variance of the ToF spectrum, with information about correlated ions appearing in the form of cross peaks away from the diagonal. Interpretation of these cross peaks has been discussed thoroughly in a number of previous publications.^{1,2,4,19,20}

Calculation of the recoil-frame covariance is complicated by the fact that the full covariance matrix between a pair of two-dimensional velocity-map images has four dimensions, making interpretation (and data storage) challenging. Instead, we use a simple procedure to reduce the dimensionality from four to two. Having selected the two velocity-map images of interest, we designate one ion as the ‘reference’ ion, and the other as the ‘signal’ ion. Since the aim is to identify any correlations between the pixel intensities within each image, we need to calculate the covariance between each pixel in the reference ion image and each pixel in the signal image, with the averaging being performed over acquisition cycles, as in the case of ToF covariance outlined above. Before performing the covariance calculation, the reference and signal images are rotated such that the reference pixel of interest always lies along a common axis. The reasons for this are two-fold: to reduce the dimensionality of the resulting covariance matrix; and to allow the covariance maps generated for each pixel to be summed as they are calculated to give an overall covariance map. The resulting recoil-frame covariance map can be interpreted (at least approximately) as showing the velocity distribution of the signal ion relative to that of the reference ion.

Note that if the calculations have been performed correctly then the integrated intensity of the recoil-frame covariance map for a given ion pair should be equal to the intensity of the corresponding cross peak in the ToF covariance map. Examples of recoil-frame covariance maps can be seen in Figures 3 and 4.

2.1.3 Contingent covariance

Contingent covariance utilises Equation 1, but groups the data into subsets based on some varying parameter, and then runs the covariance analysis on each of these groups. Within each subset, the fluctuation is small and there are correspondingly relatively few false covariances. The resulting covariance maps for each subset can then be summed to give the final covariance image. It should be noted that the contingent covariance approach does lead to a reduction in the signal-to-noise ratio achievable within the final covariance image,⁴ and this should be taken into account when deciding on the number of experimental cycles over which data should be acquired. Contingent recoil-frame covariance is trivial to implement, as the data simply need to be segmented into appropriate subsets based on the values of the variable parameter. The individual covariance maps for each subset are then summed to give the final result.

2.1.4 Partial covariance

Partial covariance adds a correction term to Equation 1 to account for the presence of a varying parameter, I . We can define the partial covariance as follows:^{4,15,16}

$$\text{pcov}(X, Y; I) = \text{cov}(X, Y) - \frac{\text{cov}(X, I) \text{cov}(I, Y)}{\text{cov}(I, I)} \quad (2)$$

Note that $\text{cov}(I, I)$ is simply the variance of I . It is also possible to extend this treatment to account for multiple varying parameters,^{4,16,17} but this is not considered further here.

When applied to recoil-frame covariance, partial covariance is a little more challenging to implement than contingent covariance. Inspecting Equation 2, the variance $\text{cov}(I, I)$ of the varying parameter can be trivially calculated, as can the two covariance terms $\text{cov}(X, I)$ and $\text{cov}(Y, I)$. However, when multiplying the two covariance terms, rather than creating a four-dimensional array, we must repeat the rotation process discussed in Section 2.1.2 in order to obtain the correct result for the second term in Equation 2.

2.2 Experimental

The application of partial and contingent ToF and recoil-frame covariance analysis is demonstrated using velocity-map imaging data from electron-molecule crossed-beam scattering experiments on the dissociative electron ionization of N_2O . The experimental setup has been discussed in detail previously,²¹ and will only be described briefly here.

To acquire the data reported here, nitrous oxide at a stagnation pressure of ~ 2 bar undergoes supersonic expansion through a pulsed solenoid valve (Hannifin-Parker Series 9 general valve) to produce a pulsed molecular beam. A pulsed electron beam from a low-energy electron gun (PSP Vacuum Technology ELS 100) is crossed with the molecular beam between the grounded repeller and extractor electrodes of a velocity-map imaging ion lens.²² After the ~ 300 ns electron beam pulse has passed through the interaction region, the repeller and extractor electrodes are rapidly pulsed to their operating potentials using a pair of fast transistor switches (Behlke model HTS-101). The resulting electric field accelerates any ions produced in the electron-molecule collisions along the flight tube towards a position-sensitive ion detector comprising a pair of chevron-mounted microchannel plates coupled to a P47 scintillator. The ion detector converts the incoming ion impacts to an optical image on the phosphor, and a Pixel Imaging Mass Spectrometry (PIImMS) camera captures the x , y , t coordinates for each detected ion. As noted above, the data are stored as a list of (x, y, t, n) data points, with n the acquisition cycle within which the ion was detected. Data were recorded for a total of 750,000 acquisition cycles.

The ToF spectrum of the fragment ions can be obtained from the PIImMS data set by integrating over the x and y coordinates, and velocity-map images for given mass-to-charge ratios are obtained by integrating over the appropriate range of ion arrival times t . ToF and recoil-frame covariance maps are constructed from the data using the methods outlined in Section 2.1.2.

3 Results and discussion

We have chosen to demonstrate the enhanced capabilities of partial and contingent covariance analysis using velocity-map imaging data on the dissociative electron ionization of N_2O . At the electron energy of 100 eV employed in the present study, the majority of collisions lead to production of singly charged N_2O^+ cations, many of which dissociate to form one ionic and one neutral

product. None of these channels give rise to covariance signals, since only the ionic products are detected in our experiment.

Around 16% of collisions²³ lead to double or even triple ionization of N_2O . Doubly-charged N_2O^{2+} can dissociate to form a number of different products, including $\text{N}_2^+ + \text{O}^+$, $\text{N}^+ + \text{NO}^+$, $\text{N}^+ + \text{N}^+ + \text{O}$, and $\text{N}^+ + \text{N} + \text{O}^+$, and we might expect to see covariance signals arising from the ion pairs formed within each of these channels.

Figure 1(a) shows the uncorrected ToF covariance map obtained following dissociative electron ionization of N_2O at an electron energy of 100 eV. We indeed see covariance signal arising from each of the doubly-charged ion fragmentation pathways listed above. These features characteristically have a negative slope as a consequence of conservation of momentum, as has been discussed in detail elsewhere.^{1,19,20} In addition to the expected covariance signals, we also see significant signal arising from false covariance, for example between the parent ion and all other ions. As explained in Section 1, these false covariances are experimental artefacts arising from fluctuations or drift in the intensities of the electron and/or molecular beams, and we might hope that they will be eliminated, or at least reduced significantly, when we employ partial or contingent covariance.

Ideally, one would monitor the molecular beam density and electron beam current during acquisition, and use these as the varying parameters when performing partial or contingent covariance. However, recording and storing this data on every acquisition cycle and ensuring correct co-registration of beam intensities and PImMS data sets for each cycle would add considerable complexity to the experimental set up. Instead, we have explored using the PImMS signal itself to define the varying parameter. Initially, we attempted to use the total ion count recorded in each acquisition cycle, shown as a function of time in Figure 2(a), as the varying parameter. However, as shown in Figure 1(b), this led to significant over-subtraction of the false covariance, manifesting as large ‘islands’ of negative intensity in the covariance map. These appear as white areas in Figure 1(b). The fact that this choice of varying parameter does not give satisfactory results is not particularly surprising; under a given set of experimental conditions, in this case defined by the electron beam energy, density and current, and the molecular beam density, there will be statistical variation in the number of ions produced between acquisition cycles, but these will be treated differently with this choice of varying parameter.

If we instead take a moving average of the ion count, shown in Figure 2(b),

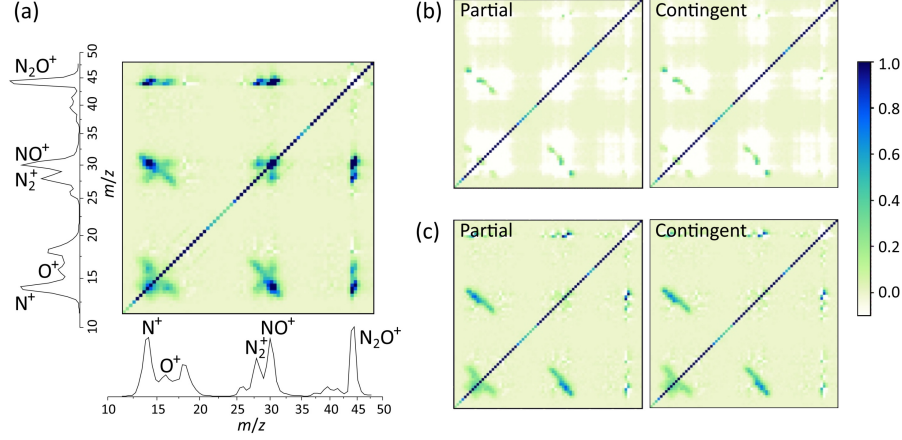


Figure 1: ToF covariance maps obtained for N_2O at an electron energy of 100 eV: (a) Uncorrected covariance map, with the fragment ToF spectrum shown along each axis; (b) partial and contingent covariance maps obtained using the total ion count recorded within each individual acquisition cycle as the varying parameter (see Figure 2(a)); (c) partial and contingent covariance maps obtained using the moving average of the total ion count as the varying parameter (see Figure 2(b)). The relative intensity scale for the maps is indicated by the colour bar.

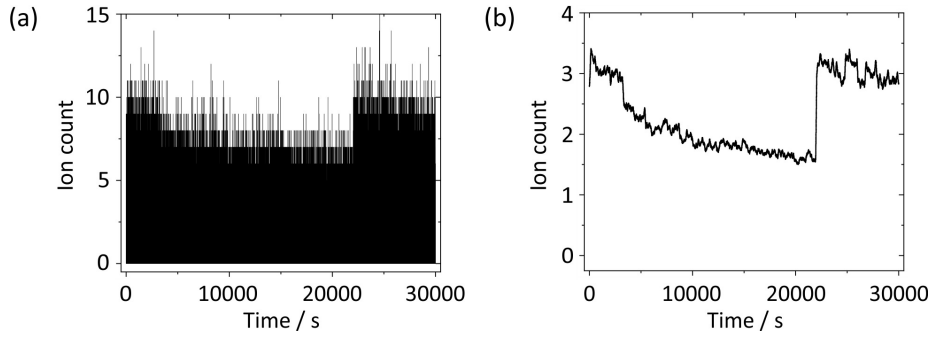


Figure 2: (a) Total ion count recorded on each acquisition cycle plotted as a function of acquisition time; (b) 100 s moving average of the total ion count recorded on each acquisition cycle plotted as a function of acquisition time.

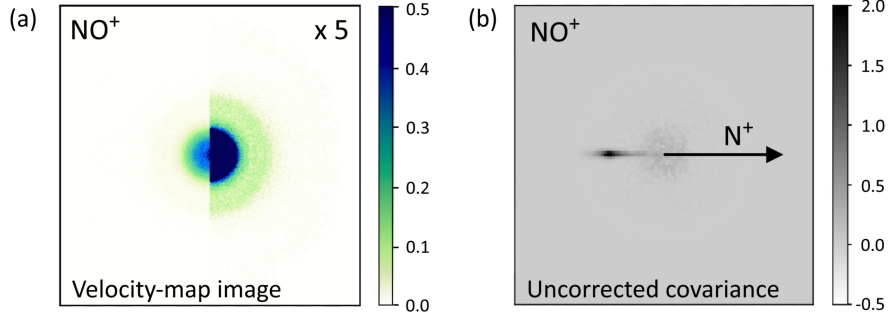


Figure 3: (a) Symmetrised velocity-map image for the NO^+ fragment ion formed in the 100 eV dissociative electron ionisation of N_2O . Two different colour scales are used for the left and right hand sides of the image in order to emphasise the inner and outer rings, corresponding to signal arising from dissociation of singly-charged and doubly-charged parent ions, respectively; (b) Uncorrected covariance image obtained for the NO^+ ion referenced to the N^+ ion. Relative intensity scales are indicated by the colour bars.

we obtain much better results. We have used a moving average over 2501 acquisition cycles, which corresponds to a time of 100 s. The number of points in the moving average was not found to be particularly critical, provided the averaging was carried out over a time period greater than one second (25 acquisition cycles). Figure 1(c) shows partial and contingent ToF covariance maps generated using the moving average of the signal as the varying parameter. We see clear off-diagonal features corresponding to the expected covariances between pairs of product ions, with vastly reduced contributions from false covariances, indicating that these have now been properly subtracted from the covariance signal. The improvement in performance is straightforward to rationalise using the same arguments as before: provided the experimental drift is on a timescale longer than that used as a moving average, the fluctuations in beam intensities will be accounted for, but the statistical variation in the number of ions produced on each cycle will be averaged out, making the moving average a much better descriptor of the variation in experimental conditions.

Now that we have established an appropriate varying parameter to use, we will demonstrate the extension of partial and contingent methods to recoil-frame covariance. Figure 3(b) shows the uncorrected recoil-frame covariance map, which comprises two major features. The first feature is a narrow line of high intensity appearing in a direction opposite to the reference direction, and is

the ‘true’ covariance signal expected for a two-body dissociation. The spread of velocities in the radial direction is caused by the fact that the two velocity-map images used to generate the covariance map are two-dimensional projections of the full three-dimensional scattering distribution for each ion. The second signal is an isotropic feature in the centre of the image. As it is apparent that this is not consistent with conservation of momentum, we can conclude that this feature arises from false covariance. If we compare the feature to the velocity-map image for the NO^+ , shown in Figure 3(a), we can confirm that this is indeed the case; the central section of the ion image, corresponding to dissociation of singly-charged N_2O , corresponds to the central feature in the covariance map. Fluctuations in this large signal with electron or molecular beam intensity result in the false covariance signal observed. Note that the dissociation channel leading to the observed recoil-frame covariance, which accounts for around 13% of the NO^+ signal,²³ is visible in the velocity-map image as a very faint ring at the same radius as the covariance signal. We have artificially amplified the intensity in one half of the velocity-map image shown in Figure 3(a) in order to accentuate this feature.

Figure 4(a) shows the partial recoil-frame covariance map obtained using the 100 s moving average of the ion count discussed above as the varying parameter. When compared with Figure 3, we see that the central feature corresponding to false covariance is now greatly reduced in intensity, showing that the partial covariance approach is just as successful when applied to recoil-frame covariance as it is for ToF covariance. The approach is able to successfully isolate the product recoil velocity distributions arising from doubly-charged parent ion fragmentation even when the vast majority ($\sim 85\%$) of signal in the original velocity-map images arises from singly-charged parent ion fragmentation.

Contingent recoil-frame covariance analysis has been carried out in two different ways. In the first, the data was sorted by acquisition cycle according to the value of the varying parameter, and the ‘ranked’ data set was then split into subsets of 50,000 acquisition cycles in order to perform the contingent covariance analysis. In the following this is referred to as ion-count contingent covariance. The results of this analysis are shown in Figure 4(b). In common with the partial covariance map, we see that the false covariance signal has been all but eliminated, indicating that partial and contingent covariance perform similarly, at least in relation to our data.

Based on the assumption that most of the false covariance arises from a relatively slow drift in the beam intensities during the acquisition, we also per-

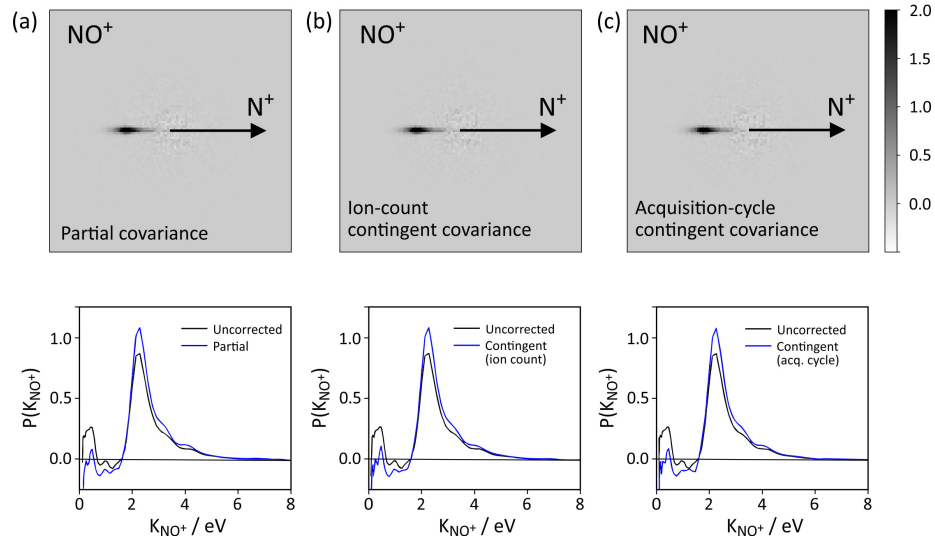


Figure 4: Recoil-frame covariance maps and NO^+ kinetic energy distributions obtained using (a) partial covariance (b) ion-count contingent covariance, and (c) acquisition-cycle contingent covariance. For (a) and (b), a 100 s moving average of the total ion count per acquisition cycle has been used as the varying parameter. For (c), the data was segmented chronologically. For both contingent covariance methods, the data set was split into subsets of 50,000 acquisition cycles each. The relative intensity scale is indicated by the colour bar.

formed a simpler version of the contingent covariance analysis. In this second approach, the data set was simply segmented chronologically in order of acquisition time, again into subsets of 50,000 acquisition cycles i.e. the acquisition cycle number was effectively used as the varying parameter. The results of this acquisition-cycle contingent covariance analysis are shown in Figure 4(c), and appear virtually indistinguishable from the partial covariance and ion-count contingent covariance maps. We note that this last approach is only likely to be successful in cases where experimental drift is relatively slow, though it may be possible to accommodate faster variations by reducing the number of acquisition cycles used in each subset employed for the contingent covariance analysis.

The kinetic energy distributions for the NO^+ fragments determined from the uncorrected and corrected covariance-map images are shown below the images in Figure 4. We see that the intensity at low kinetic energies arising from false covariances is reduced substantially, mostly to values below zero, in all three cases. The signal arising from fragmentation of doubly-charged N_2O^{2+} parent ions appears as an intense peak spanning the energy range from ~ 2 to 4 eV. The relatively broad nature of this peak implies significant internal excitation of the NO^+ molecular ion.

Figure 5 shows recoil-frame partial covariance-map images for all four observed dissociation channels of the doubly-charged N_2O^+ parent ion:

- (i) $\text{N}_2\text{O}^{2+} \longrightarrow \text{N}^+ + \text{NO}^+$;
- (ii) $\text{N}_2\text{O}^{2+} \longrightarrow \text{N}_2^+ + \text{O}^+$;
- (iii) $\text{N}_2\text{O}^{2+} \longrightarrow \text{N}^+ + \text{N}^+ + \text{O}$;
- (iv) $\text{N}_2\text{O}^{2+} \longrightarrow \text{N}^+ + \text{N} + \text{O}^+$.

Recoil-frame covariance-map images for the four channels obtained using all four techniques described in this paper can be found in the Supplementary Information.

Channels (i) and (ii) each correspond to a straightforward two-body dissociation, in which we expect the two charged products to recoil with equal and opposite momenta. This behaviour is immediately evident in the covariance-map images for these channels. The covariance signal in each case comprises a well-defined spot in the opposite direction to the recoil velocity of the reference ion, again with the characteristic ‘tail’ towards the centre of the image caused by the two-dimensional projection of the product scattering distributions onto the detector during the measurement. In contrast, channels (iii) and (iv) correspond to three-body decays, in which we measure only the two charged products. In both cases the decay is likely to be stepwise, with the doubly-charged parent

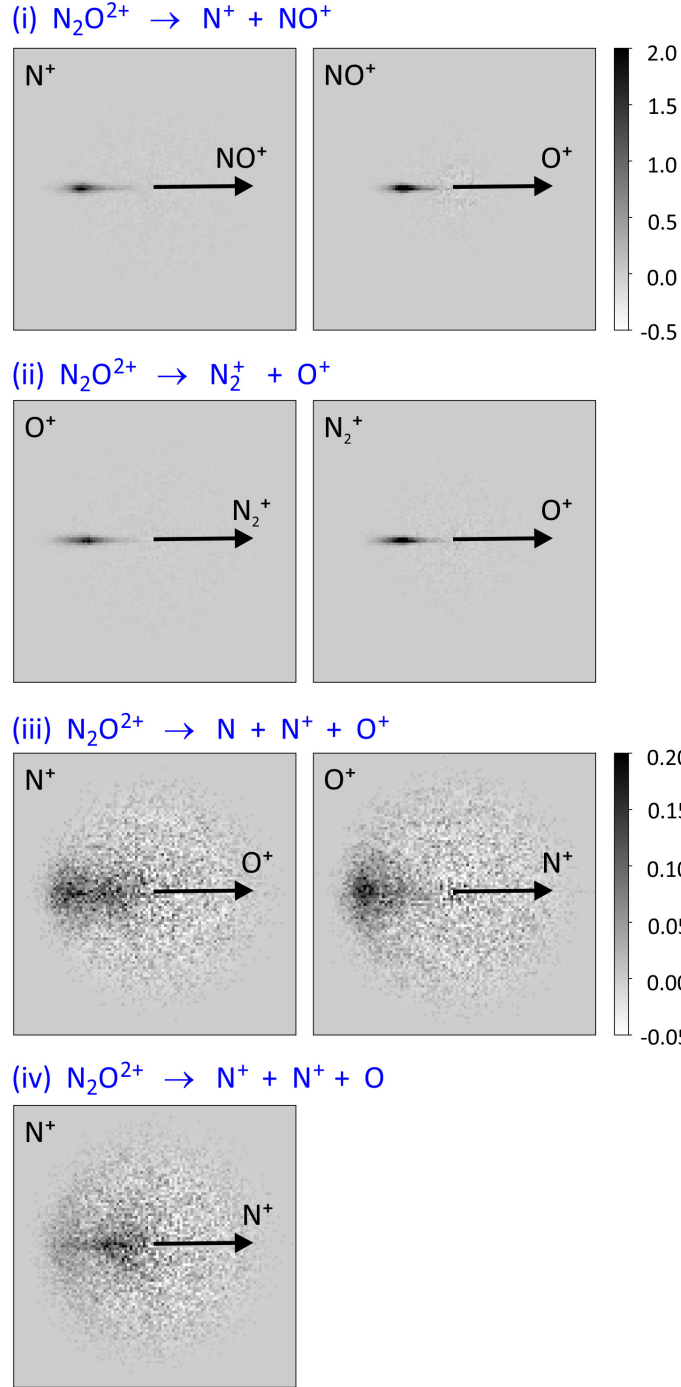


Figure 5: Recoil-frame covariance maps obtained using partial covariance for the four observed dissociation channels of doubly-charged N_2O^{2+} ions: (i) $\text{N}_2\text{O}^{2+} \rightarrow \text{N}^+ + \text{NO}^+$; (ii) $\text{N}_2\text{O}^{2+} \rightarrow \text{N}_2^+ + \text{O}^+$; (iii) $\text{N}_2\text{O}^{2+} \rightarrow \text{N} + \text{N}^+ + \text{O}^+$; (iv) $\text{N}_2\text{O}^{2+} \rightarrow \text{N}^+ + \text{N} + \text{O}$. The relative intensity scale is indicated by the colour bar.

ion either losing the neutral fragment and then dissociating into two charged products, or dissociating into two charged products, one of which subsequently loses a neutral fragment. In either case, the momentum ‘kick’ associated with loss of the neutral fragment leads to substantial broadening of the correlation between the velocities of the two charged products, and correspondingly much less well-resolved signals in the recoil-frame covariance maps. We have shown previously^{1,5} that if the energetics of the two steps in the dissociation mechanism are known at least approximately, simulations of the expected covariance maps for the two possible mechanisms can be used to distinguish between them. However, we have not yet performed this analysis for N_2O , and will report on details of the dissociation mechanisms associated with each channel in a future publication.

We note that as with ToF covariance, it is also possible to combine both partial and contingent covariance approaches when performing recoil-frame covariance analysis. This involves slicing the data into subsets based on the varying parameter, and then applying the partial covariance correction within each subset. This was not found to be necessary for the data presented here, but may be very helpful in reducing contributions from false covariance in cases where there is a significant non-linear dependence of the signal on the varying parameter. To achieve this, the data subsets should be chosen such that the parameter can be approximated as varying linearly within the range covered by the subset.

4 Conclusions

We have shown that partial and contingent covariance approaches can be applied both to time-of-flight data and to velocity-map imaging data recorded in a crossed-beam scattering experiment. Both approaches are highly successful in removing false covariance signals arising from experimental drift. We have also shown that the overall ion signal can be used to generate a suitable varying parameter for use in these analyses, eliminating the need for separate measurements of experimental parameters such as beam intensities. Our approach is general, and applicable to data from any velocity-map imaging experiments in which multiple products are detected from a chemical process of interest.

Supplementary Information

The Supplementary Information contains recoil-frame covariance maps for all four observed fragmentation channels of doubly-charged N_2O^{2+} ions: (i) $\text{N}_2\text{O}^{2+} \longrightarrow \text{N}^+ + \text{NO}^+$; (ii) $\text{N}_2\text{O}^{2+} \longrightarrow \text{N}_2^+ + \text{O}^+$; (iii) $\text{N}_2\text{O}^{2+} \longrightarrow \text{N}^+ + \text{N}^+ + \text{O}$; and (iv) $\text{N}_2\text{O}^{2+} \longrightarrow \text{N}^+ + \text{N} + \text{O}^+$. In each case, covariance maps have been generated using each of the four different covariance methods described in the main text (‘uncorrected’ covariance, partial covariance, ion-count contingent covariance, and acquisition cycle contingent covariance).

Acknowledgements

This work was supported by the EPSRC under Programme Grants EP/L005913/1 and EP/T021675/1.

References

- [1] Vallance, C.; Heathcote, D.; Lee, J. W. L. Covariance-Map Imaging: A Powerful Tool for Chemical Dynamics Studies. *J. Phys. Chem. A* **2021**, *125*, 1117–1133.
- [2] Frasinski, L. J.; Codling, K.; Hatherly, P. A. Covariance mapping: A correlation method applied to multiphoton multiple ionization. *Science* **1989**, *246*, 1029–1031.
- [3] Bhardwaj, V. R.; Vijayalakshmi, K.; Mathur, D. Dissociative ionization of benzene in intense laser fields of picosecond duration. *Phys. Rev. A* **1999**, *59*, 1392.
- [4] Frasinski, L. J. Covariance mapping techniques. *J. Phys. B* **2016**, *49*, 152004.
- [5] Köckert, H.; Heathcote, D.; Lee, J. W. L.; Vallance, C. Covariance-map imaging study into the fragmentation dynamics of multiply-charged CF_3I formed in electron-molecule collisions. *Mol. Phys.* **2021**, *119*, e1811909.
- [6] Slater, C. S.; Blake, S.; Brouard, M.; Lauer, A.; Vallance, C.; John, J. J.; Turchetta, R.; Nomerotski, A.; Christensen, L.; Nielsen, J. H. et al. Covariance imaging experiments using a pixel-imaging mass-spectrometry camera. *Phys. Rev. A* **2014**, *89*, 11401.

- [7] Slater, C. S.; Blake, S.; Brouard, M.; Lauer, A.; Vallance, C.; Bohun, S.; Christensen, L.; Nielsen, J. H.; Johansson, M. P.; Stapelfeldt, H. Coulomb explosion imaging using a Pixel Imaging Mass Spectrometry camera. *Phys. Rev. A* **2015**, *91*, 053424.
- [8] Bargheer, M.; Zhavoronkov, N.; Woerner, M.; Elsaesser, T. Recent progress in ultrafast X-ray diffraction. *ChemPhysChem* **2006**, *7*, 783.
- [9] Burt, M.; Amini, K.; Lee, J. W. L.; Christiansen, L.; Johansen, R. R.; Kobayashi, Y.; Pickering, J. D.; Vallance, C.; Brouard, M.; Stapelfeldt, H. Gas-phase structural isomer identification by Coulomb explosion of aligned molecules. *J. Chem. Phys.* **2018**, *148*, 091102.
- [10] Amini, K.; Boll, R.; Lauer, A.; Burt, M.; Lee, J. W. L.; Christensen, L.; Brausse, F.; Mullins, T.; Savelyev, E.; Abttdkim, U. et al. Alignment, orientation, and Coulomb explosion of difluoriodobenzene studied with the pixel imaging mass spectrometry (PImMS) camera. *J. Chem. Phys.* **2017**, *147*, 013933.
- [11] Hansen, J. L.; Nielsen, J. H.; Madsen, C. B.; Lindhardt, A. T.; Johansson, M. P.; Skrydstrup, T.; Madsen, L. B.; Stapelfeldt, H. Control and femtosecond time-resolved imaging of torsion in a chiral molecule. *J. Chem. Phys.* **2012**, *136*, 204310.
- [12] Pickering, J. D.; Shepperson, B.; Hubschmann, B. A. K.; Thorning, F.; Stapelfeldt, H. Alignment and imaging of the CS₂ dimer inside helium nanodroplets. *Phys. Rev. Lett.* **2018**, *120*, 113202.
- [13] Pickering, J. D.; Shepperson, B.; Christiansen, L.; Stapelfeldt, H. Alignment of the CS₂ dimer embedded in helium droplets induced by a circularly polarised laser pulse. *Phys. Rev. A* **2019**, *99*, 043403.
- [14] Schouder, C.; Chatterley, A. S.; Calvo, F.; Christiansen, L.; Stapelfeldt, H. Structure determination of the tetracene dimer in helium nanodroplets using femtosecond strong-field ionization. *Struct. Dyn.* **2019**, *6*, 044301.
- [15] Frasninski, L. J.; Giles, A. J.; Hatherly, P. A.; Posthumus, J. H.; Thompson, M. R.; Codling, K. Covariance mapping and triple coincidence techniques applied to multielectron dissociative ionization. *J. Electron Spect. Rel. Phenom.* **1996**, *79*, 367–371.

- [16] Krzanowski, W. J. *Principles of multivariate analysis : a user's perspective*; Oxford statistical science series; Oxford University Press, 2000.
- [17] Zhaunerchyk, V.; Frasninski, L. J.; Eland, J. H. D.; Feifel, R. Theory and simulations of covariance mapping in multiple dimensions for data analysis in high-event-rate experiments. *Phys. Rev. A* **2014**, *89*, 53418.
- [18] Mikosch, J.; Patchkovskii, S. Coincidence and covariance data acquisition in photoelectron and ion spectroscopy. I. Formal theory. *J. Mod. Opt.* **2013**, *60*, 1426.
- [19] Eland, J. H. D.; Wort, F. S.; Royds, R. N. A photoelectron-ion-ion triple coincidence technique for the study of double photoionization and its consequences. *J. Electron Spect. Rel. Phenom.* **1986**, *41*, 297–309.
- [20] Eland, J. H. D. The dynamics of three-body dissociations of dications studied by the triple coincidence technique PEPIPICO. *Mol. Phys.* **1987**, *61*, 725–745.
- [21] Köckert, H.; Heathcote, D.; Lee, J. W. L.; Zhou, W.; Richardson, V.; Vallance, C. C-I and C-F bond-breaking dynamics in the dissociative electron ionization of CF₃I. *Phys. Chem. Chem. Phys.* **2019**, *21*, 14296–14305.
- [22] Eppink, A. T. J. B.; Parker, D. H. Velocity map imaging of ions and electrons using electrostatic lenses: Application in photoelectron and photofragment ion imaging of molecular oxygen. *Rev. Sci. Instrum.* **1997**, *68*, 3477–3484.
- [23] Love, N. A.; Price, S. D. Electron ionization of N₂O. *Phys. Chem. Chem. Phys.* **2004**, *6*, 4558–4565.